Synthesis of Multishell Nanoplates by Consecutive Epitaxial Growth of Bi_2Se_3 and Bi_2Te_3 Nanoplates and Enhanced Thermoelectric Properties

Yuho Min,[†] Gyeongbae Park,[‡] Bongsoo Kim,[†] Anupam Giri,[‡] Jie Zeng,[§] Jong Wook Roh,[∥] Sang Il Kim,[∥] Kyu Hyoung Lee,*[,⊥] and Unyong Jeong*[,‡]

[†]Department of Materials Science and Engineering, Yonsei University, 134 Shinchon-dong, Seoul 120-749, Korea, [‡]Department of Materials Science and Engineering, Pohang University of Science and Technology (POSTECH), 77 Cheongam-Ro, Nam-Gu, Pohang 790-784, Korea, [§]Hefei National Laboratory for Physical Sciences at the Microscale & Collaborative Innovation Center of Suzhou Nano Science and Technology, University of Science and Technology of China, Hefei, Anhui 230026, P. R. China, [∥]Materials Research Center, Samsung Advanced Institute of Technology, Samsung Electronics, Suwon 443-803, Korea, and [⊥]Department of Nano Applied Engineering, Kangwon National University, Chuncheon 200-701, Korea

ABSTRACT We herein demonstrate the successive epitaxial growth of Bi_2Te_3 and Bi_2Se_3 on seed nanoplates for the scalable synthesis of heterostructured nanoplates (Bi_2Se_3@Bi_2Te_3) and multishell nanoplates (Bi_2Se_3@Bi_2Te_3@Bi_2Se_3, Bi_2Se_3@Bi_2Te_3@Bi_2Se_3@Bi_2Te_3). The relative dimensions of the constituting layers are controllable *via* the molar ratios of the precursors added to the seed nanoplate solution. Reduction of the precursors produces nanoparticles that attach preferentially to the sides of the seed nanoplates. Once attached, the nanoparticles reorganize epitaxially on the seed crystal lattices to form single-crystalline core–shell nanoplates. The nanoplates, initially 100 nm wide, grew laterally to 620 nm in the multishell structure, while their thickness increased more moderately, from 5 to 20 nm. The nanoplates were pelletized into bulk samples by spark plasma sintering and their thermoelectric properties are compared. A peak thermoelectric figure of merit (ZT) ~0.71 was obtained at 450 K for the bulk of Bi_2Se_3@Bi_2Te_3 nanoplates by simultaneous modulation of electronic and thermal transport in the presence of highly dense grain and phase boundaries.

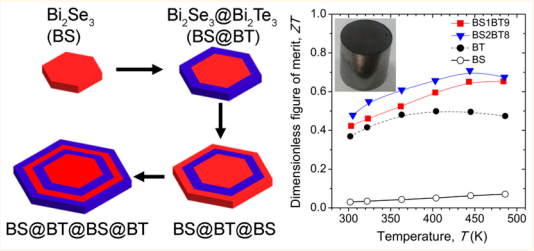

KEYWORDS: two-dimensional materials · seeded growth · core–shell nanoplates · multishell nanoplates · Bi_2Se_3 · Bi_2Te_3 · thermoelectric properties

A high degree of control over the size, structure, and composition of nanocrystals is essential to tune their chemical and physical properties for target applications.[1−4] In particular, 2D nanocrystals of different sizes have been investigated extensively owing to their superior electrical, optical, and thermal properties.[5−13] In this context, much effort has recently been devoted to the production of a wide range of homogeneous 2D nanocrystals *via* solution-based synthesis.[14−23] This preparation route is also interesting for more complicated systems, heterogeneous in chemical composition and structure. Indeed, heterostructured nanocrystals are expected to provide unconventional but valuable properties that are not provided by homogeneous 2D nanocrystals.[24] However, reports on the solution-based synthesis of heterogeneous 2D nanocrystals are sparse in the literature. Previous efforts have mainly focused on the fabrication of Cd-containing core/shell nanoplatelets.[24−26] A rational method for the solution-based synthesis of various 2D heterostructures is therefore of substantial interest.

Multilayered structures with precisely controlled dimensions and composition are essential in a number of areas of both fundamental and applied research.[27] In this context, thin films have successfully been grown epitaxially under vacuum with atomic-level control over their thickness.[28,29] However, solution-based synthesis provides better control over epitaxial growth in the lateral direction, notably for the formation of 2D heterostructured materials. Unfortunately,

* Address correspondence to ujeong@postech.ac.kr, khlee2014@kangwon.ac.kr.

Received for review December 19, 2014 and accepted July 2, 2015.

Published online July 02, 2015
10.1021/nn507250r

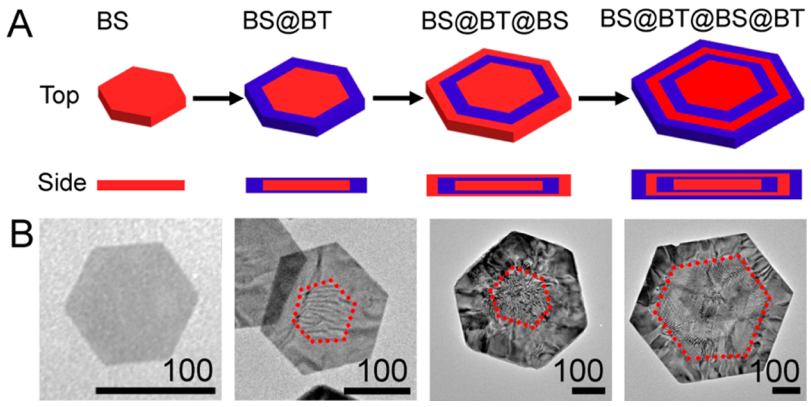

Figure 1. (A) Evolution of the seed Bi_2Se_3 (BS) nanoplates into core−shell, double-shell, and multishell bismuth chalcogenide nanoplates Bi_2Se_3@Bi_2Te_3@Bi_2Se_3@Bi_2Te_3 (BS@BT@BS@BT). (B) Typical transmission electron micrographs obtained from the nanoplates whose assembly is outlined in (A). The areas enclosed in red dotted line show Moiré patterns.

the chemical composition, shape, and dimensions of these materials are difficult to control such that the resulting structures are often not those targeted.[30,31] Well-defined laterally heterostructured 2D nanocrystals are only obtained if lateral growth is favored and vertical growth restricted. Anisotropic control over the surface energy is required, unlike for spherical nanoparticles on which multiple coatings have been successfully been deposited.[32,33] Large differences in lattice size or interfacial energy should be avoided as they lead to nonconformal growth and cause crystal defects.[25,31,34] Mutual diffusion of elements at the interface is another concern since it can lead to the formation of alloys or compounds.[35]

Herein, we demonstrate the solution-based synthesis of 2D heterostructured nanomaterials with multiple laterally grown epitaxial layers. For a proof-of-concept experiment, we chose Bi_2Se_3 and Bi_2Te_3 as the constituents of the heterostructure. Bismuth chalcogenides (Bi_2Q_3, Q = Se, Te) are layer-structured materials arranged in planar quintuple layers (QLs, with each QL approximately 1 nm thick). Each QL consists of five consecutive covalently bound atomic sheets (Q−Bi−Q−Bi−Q), and neighboring QLs are stacked by weak van der Waals interactions along the *c*-axis.[36] They are isomorphic with only small differences in lattice distances, so the epitaxial growth of one constituent is possible on the other.

In terms of practical applications, the interest in 2D bismuth chalcogenides (Bi_2Se_3, Bi_2Te_3) lies in their thermoelectric properties and in the unique surface electronic states that make these materials topological insulators.[37−45] It is well-known that introducing nanoscale grains and interfaces in nanostructured bulk composites increases the phonon scattering and filters low energy charge carriers without any considerable reduction in electronic conductivity. This enhanced phonon scattering leads to a higher thermoelectric figure of merit (ZT).[46,47] As previously demonstrated by our group, ZT can be improved simply by mixing Bi_2Se_3 and Bi_2Te_3 nanoflakes.[37] However, Bi_2Te_3 nanoplates or nanoflakes tend to aggregate such that nanoscale interfaces are not homogeneously distributed throughout the sample. One promising approach for achieving uniformly distributed nanoscale interfaces is to use laterally heterostructured nanoplates as building blocks. In this study, we investigated thermoelectric properties of pelletized bulk samples made of the $(Bi_2Se_3)_x$@$(Bi_2Te_3)_{1-x}$ heterostructured nanoplates with different relative dimensions between the core and shell. The pelletized bulk of $(Bi_2Se_3)_2$@$(Bi_2Te_3)_8$ nanoplates showed a peak ZT of 0.71 at 450 K.

RESULTS AND DISCUSSION

The synthetic protocol is illustrated stepwise in Figure 1A. BT is grown epitaxially on the BS seed nanoplates, predominantly on the side surfaces owing to its intrinsic preference for 2D growth, with only a small fraction coated on the basal planes (the top and bottom faces). This anisotropic deposition results in the formation of BS@BT core/shell nanoplates. BS is then grown epitaxially on the outer surfaces of the BS@BT structures, leading to the formation of BS@BT@BS double-shell nanoplates. A final BT shell is then added, producing BS@BT@BS@BT multishell nanoplates. Such stepwise epitaxial growth is based on an extensive characterization to follow later on and it will be discussed in detail. Figure 1B shows TEM images of the nanoplates obtained using the procedure illustrated in Figure 1A. The Moiré patterns observed in the core regions of the nanoplates (within the dotted lines) indicate that the cores overlap with a shell layer that has different lattice distances or a different crystal orientation. The lateral dimensions of the newly generated shells can be optimized by adjusting the precursor and seed-nanoplate concentrations. Table 1 compares the elemental compositions of the precursors and of the resulting nanoplates, as measured by ICP-OES. The atomic fractions added in the solution and the atomic fractions measured in the products are

in good agreement. This one-pot approach can furthermore be scaled up as required.

Bi_2Se_3 Nanoplates. The synthesis of the BS nanoplate seed crystals involves dissolving stoichiometric amounts of $Bi(NO)_3 \cdot 5H_2O$ and Na_2SeO_3 precursors, PVP, and acetic acid, in EG. The reaction is triggered at 165 °C by the rapid injection of a hydroxylamine solution (NH_2OH, 50% in H_2O, 1.2 mL in 10 mL of EG). The initially transparent mixture turns light-yellow as it is heated and then dark purple immediately after this injection. Figure 2A outlines the growth mechanism of the BS nanoplates, and Figure 2B–D shows TEM images obtained at different stages of growth. Aliquots (1 mL) were collected from the reaction batch using a needle, and the reaction was stopped by injecting aliquots into a cold vial kept in an ice bath. A large number of small BS nanoparticles nucleate within 10 s (Figure 2B), and they are attached into aggregates. The aggregates begin to transform into hexagonal nanoplates after 1 min (Figure 2C). The fast random attachment of nanoparticles causes misorientations in the growing nanoplates (Figure 2D), but thermal aging in the solution batch for 2 min facilitates the rearrangement of the atoms and generates well-defined single-crystalline BS nanoplates with clean surfaces (Figure 2E). The reaction was prolonged for 8 min beyond the typically completion time of 2 min, after which no further change was observed in the size and shape of the nanoplates. This result is consistent with our previous report on the growth mechanism of BS nanodiscs.[36] In BS, five covalently bonded atomic sheets (*e.g.*, Se–Bi–Se–Bi–Se) make one quintuple layer (QL) (~1 nm). Each QL is weakly bonded by van der Waals interaction along the [0001] direction (*c*-axis). This anisotropic bonding nature facilitates the BS to preferentially grow into 2D geometry. Figure 2F shows that the BS nanoplates are 100 ± 9 nm wide, with a highly uniform (5 nm) thickness, which indicates that most of the BS nanoplates consist of five QLs (Figure 2F). The hexagonal lattice fringe in HRTEM image clearly shows a lattice spacing of 0.21 nm, corresponding to the $(11\bar{2}0)$ lattice plane (Supporting Information, Figure S1A). Corresponding Fast Fourier Transform (FFT) pattern is indexed as [0001] zone axis, indicating that BS nanoplates consist of $(11\bar{2}0)$ and (0001) planes as side and basal planes, respectively. Powder X-ray diffractogram shows that the BS nanoplates have the rhombohedral crystalline structure in the space group of $R\bar{3}m$ (JCPDS 33-0214) (Supporting Information, Figure S1B).

TABLE 1. Elemental Compositions of the Nanoplates Synthesized in This Study[a]

	molar fractions (%)			
samples (intended molar ratio)	Bi	Se	Te	Measured compositions
BS	0.41	0.59	0	$Bi_{2.1}Se_{2.9}$
BS/BT ([BS]:[BT] = 1:4)	0.41	0.12	0.47	$(Bi_2Se_3)_{1.0}(Bi_2Te_3)_{4.0}$
BS/BT/BS ([BS]:[BT]:[BS] = 1:4:16)	0.41	0.48	0.11	$(Bi_2Se_3)_{17}(Bi_2Te_3)_{4.0}$
BS/BT/BS ([BS]:[BT]:[BS] = 1:4:32)	0.40	0.54	0.06	$(Bi_2Se_3)_{33}(Bi_2Te_3)_{4.0}$
BS/BT/BS/BT ([BS]:[BT]:[BS]:[BT] = 1:4:32:48)	0.42	0.23	0.35	$(Bi_2Se_3)_{33}(Bi_2Te_3)_{50}$

[a] The compositions were measured by ICP-OES analysis.

Bi_2Se_3@Bi_2Te_3 Core–Shell Nanoplates. The BS@BT nanoplates were synthesized through the epitaxial growth of BT on the BS nanoplates. With a 1:4 molar ratio

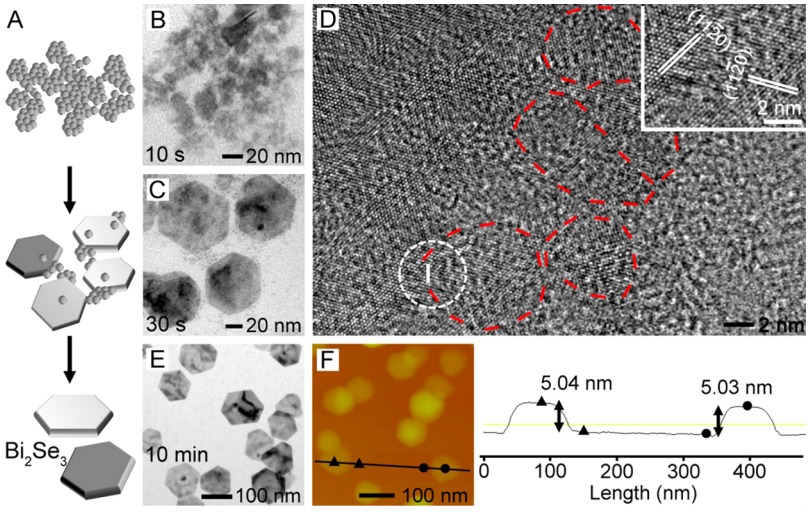

Figure 2. (A) Schematic representation of the growth mechanism of the Bi_2Se_3 nanoplates, from small nanoparticles into well-defined 6-fold symmetric nanoplates by random attachment and reorganization. (B and C) Transmission electron micrographs taken at different reaction time intervals: (B) 10 s; (C) 30 s. (D) High-resolution transmission electron micrograph obtained from the edge of the BS nanoplates highlighting crystal growth through oriented attachment. The inset shows a magnified image of the circled area marked in (D). (E) Transmission electron micrograph of the final Bi_2Se_3 nanoplates obtained after a reaction time of 10 min. (F) Atomic force micrograph (left) and the corresponding height profile (right) along the solid line drawn across the image. The measured thickness of each nanoplate is ~5 nm.

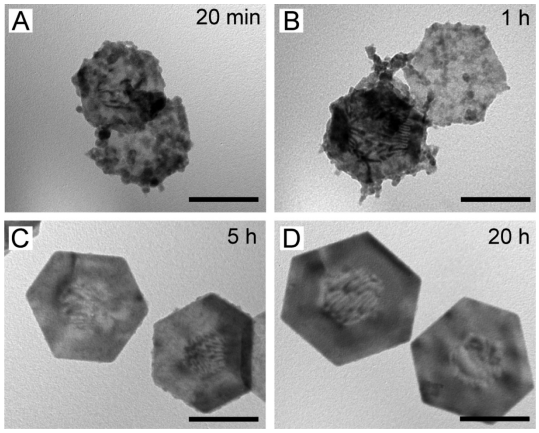

Figure 3. (A–D) Transmission electron micrographs of aliquots extracted (A) 20 min, (B) 1 h, (C) 5 h, and (D) 20 h after the addition of the Bi_2Te_3 precursor to the Bi_2Se_3 seed suspension. The scale bars in all the images represent 100 nm.

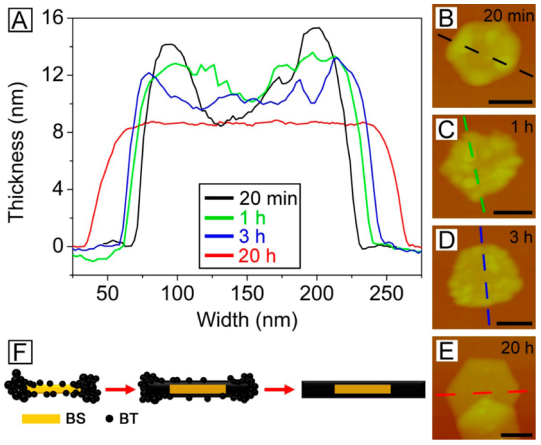

Figure 4. (A) Width and thickness, obtained by atomic force microscopy, of the nanoplates at different stages of the growth of the BT shell on the existing BS nanoplate. The profiles correspond to the dashed lines in (B–E) the micrographs obtained after (B) 20 min, (C) 1 h, (D) 3 h, and (E) 20 h. In each case, the scale bar represents 100 nm. (F) Schematic illustration of the growth mechanism during the reaction.

([BS]:[BT] = 1:4), stoichiometric amounts of $Bi(NO)_3 \cdot 5H_2O$ and Na_2TeO_3 precursors were added, together with PVP and NH_2OH, to the as-synthesized solution of BS nanoplates at room temperature. The solution was then heated to 160 °C under nitrogen atmosphere for the reaction to proceed for 24 h. The synthetic condition of Bi_2Te_3 on the premade Bi_2Se_3 core is slightly different (please see the Experimental Section for details). The Bi_2Se_3 seeds were prepared by rapidly injecting a reducing agent (hydroxylamine) into the reaction batch at 165 °C, which led to burst nucleation and growth of Bi_2Se_3 nanoplates within 10 min. To guarantee epitaxial growth of Bi_2Te_3 on the Bi_2Se_3 seeds without any homogeneous nucleation and growth of Bi_2Te_3 crystals, we added a reducing agent (hydroxylamine) to the Bi_2Se_3 suspension at room temperature and then slowly raised the solution temperature to 160 °C. Since the reduction rate of the Te precursor is lower than that of the Se precursor, the epitaxial growth was much slower than the synthesis of Bi_2Se_3 seed crystals. Scalable production was readily achieved by simply increasing the reaction volume; for example, 5.2 g of BS@BT nanoplates was produced from a 1.5 L reaction batch (Supporting Information, Figure S2). Note that the reaction should be conducted above 140 °C. Below this temperature, the Te precursor is reduced much faster than the Bi one, leading to the formation of Te nanowires first and then they are transformed into Bi_2Te_3. Therefore, the final product is a mixture of Bi_2Te_3 nanowires and nanoplates. The morphology of the samples prepared at 120 °C is shown in the Supporting Information (Figure S3).

Figure 3 shows the evolution of the shape of the BS@BT nanoplates with increasing reaction times. A large number of BT nanoparticles are generated once the reaction temperature reaches 160 °C, and within 20 min, a majority of the nanoparticles attach to the edges and side facets of the BS nanoplates, while a small number are deposited on the basal planes (Figure 3A). The covalent interactions on the side surfaces are more favorable for attachment than the weak van der Waals forces that govern attraction to the basal planes. After 1 h, Figure 3B shows that the nanoplates have grown laterally. This indicates that the BT nanoparticles initially attached to the side facets reorganize allowing epitaxial growth with the BS seed nanoplates. After 5 h, the surface roughness of the nanoplates is remarkably reduced and a clear hexagonal structure becomes apparent (Figure 3C). The appearance of a Moiré pattern in the core region indicates that the BT nanoparticles adsorbed on the basal planes reorganize and coat the surface of the BS seeds. This process is complete after 20 h while the definition of the hexagonal BS@BT nanoplates is further improved (Figure 3D).

The slow growth rate of these nanoplates facilitates the microscopic analysis of the stepwise evolution of the nanoplates. Figure 4A shows the variation in thickness and width across the BS@BT nanoplates at different stages of formation. Representative AFM images among those obtained from 10 different samples at each reaction time are shown in Figure 4B–D. Because under these reaction conditions the Bi and Te precursors are completely reduced within 10 min, it is reasonable to assume that the reorganization of the BT nanoparticles on the seeds occurs without any additional deposition of atoms from the solution. After 20 min, the edges and the central area of the nanoplates are found to be ~15 nm and ~11 nm thick, respectively, with a caldera-like topology (the black profile in Figure 4A) that indicates that the BT nanoparticles attach mostly to the side surfaces. After 1 h, the nanoplates became thinner, ~13 nm thick on their edges and ~9 nm thick in their centers, but wider, their lateral dimensions having grown from ~160 to ~180 nm (the black and green profiles in Figure 4A).

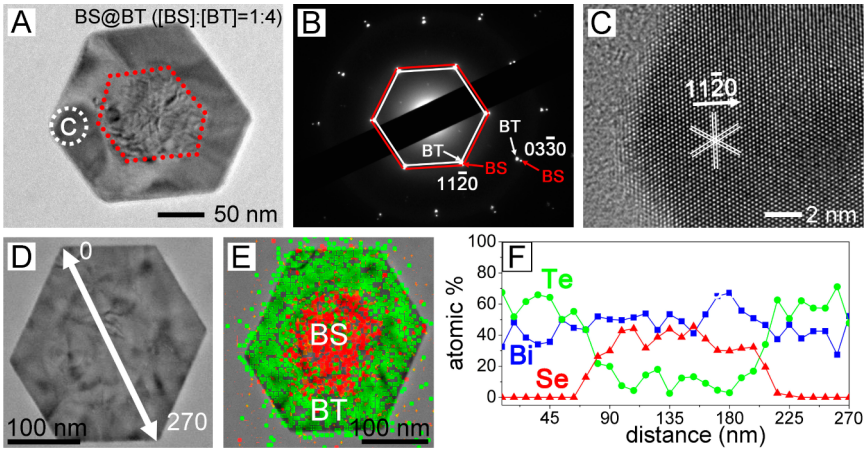

Figure 5. (A) Transmission electron microscopy (TEM) image and (B) the corresponding selected area diffraction pattern of a Bi_2Se_3@Bi_2Te_3 (BS@BT) core/shell nanoplates synthesized at a molar ratio ([BS]:[BT]) of 1:4. (C) High-resolution TEM image of the area circled in panel (A), showing the (11$\bar{2}$0) planes of BT. (D) Scanning TEM image of a single BS@BT nanoplate and (E) the corresponding Se (red) and Te (green) maps obtained by energy dispersive X-ray spectroscopy. (F) Elemental profile measured along the arrow shown in panel (D).

This suggests that the BT nanoparticles initially deposited on the basal planes migrate to the edges and contribute to lateral growth. The large variation in thickness of the central area reflects the presence of BT nanoparticles on the BS surfaces. The evolution up to a reaction time of 3 h follows the same trend, with the nanoplates thinning to ~12 nm on their edges and ~10 nm in their center, and widening slightly to ~190 nm (the blue profile in Figure 4A). The AFM image in Figure 4D shows that at this stage, the reorganization of the BT nanoparticles on the basal planes is still in progress. After 5 h, the formation of the nanoplates is complete and no further changes are observed up to 20 h. The nanoplates are ~210 nm wide with a constant thickness of ~8 nm (the red profile in Figure 4A). Accounting for the thickness of the BS nanoplates and of the BS@BT nanoplates, this additional BT coating must consist of 1 or 2 QLs. A representative AFM image of the nanoplates at this stage is shown in Figure 4E. On the basis of these TEM and AFM results, a growth mechanism for BT shell is proposed, as outlined in Figure 4F. Initially, the BT nanoparticles attach mainly to the edges but also to the surfaces of the nanoplates. These then reorganize allowing epitaxial growth in the lateral direction. The BT nanoparticles on the basal planes migrate to the edges, and reorganize across the BS surface producing a uniform coating.

Figure 5 reveals the crystal structures of the BS@BT nanoplates shown in Figure 3D, obtained with a [BS]:[BT] molar ratio of 1:4. Moiré patterns, as shown in Figure 5A and highlighted within the red dotted line, were observed for most of the nanoplates. The presence of Moiré patterns, which arise when two crystals overlap with mechanical stress at the interface,[48] implies that the core BS nanoplates are covered with crystalline BT layers and that the two structures have different lattice distances. The selected area electron diffraction (SAED) pattern (Figure 5B), obtained from the core/shell nanoplate shown in Figure 5A, reveals two regions of 6-fold symmetry along the [0001] zone axis. These diffraction points are indexed to the (11$\bar{2}$0) and (03$\bar{3}$0) planes of BT and BS. This SAED image verifies that BT grows epitaxially on the BS nanoplates. Figure 5C shows the high resolution TEM image taken from the position marked with a dashed circle in Figure 5A. The lattice distance of 0.218 nm measured on the outer edge corresponds to the lattice distance between the (11$\bar{2}$0) planes of BT. The small lattice mismatches (~5%), for the lateral (11$\bar{2}$0) and vertical (000l) planes, allow epitaxial growth. The scanning TEM images and the EDS maps in Figure 5D,E highlight the structure of the BS@BT nanoplates, with a BS core (the red region in Figure 5E) and a BT shell (the green region in Figure 5E). Additionally, Figure S4 in the Supporting Information clearly shows the elemental distribution of core–shell nanoplates with individual maps of constituent elements. In the elemental profile (Figure 5F) measured along the line indicated in Figure 5E, Se is detected only in the core of the nanoplate, Te is the main element present in the shell and makes up a small proportion of the core, while a similar percentage of Bi is detected across the nanoplate. Te and Bi are present in stoichiometric proportions in the shell, with on average 60 and 40 atom %, respectively. The core consists of Se (~45 at%), Te (~15 at%), and Bi (~40 at%), confirming that the BS nanoplates are coated with BT. The above results all demonstrate the successful formation of BS@BT core–shell nanoplates. The lateral dimension and composition of BS@BT core–shell nanoplates were controllable by simply adjusting the molar ratios of the BT precursors added to the BS seed solution. Figure S5 in the Supporting Information shows the BS@BT core–shell nanoplates with a relative composition of [BS]:[BT] = 1:9. The nanoplates had a

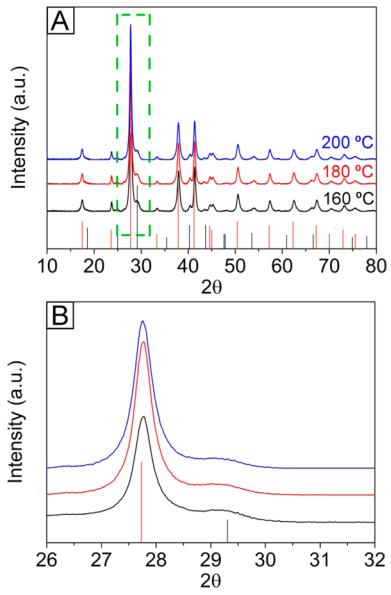

Figure 6. (A) X-ray diffractogram of Bi_2Se_3@Bi_2Te_3 (BS@BT) core/shell nanoplates prepared at different temperatures, along with the standard JCPDS data for rhombohedral Bi_2Te_3 (15-0863, red) and Bi_2Se_3 (33-0214, black). (B) Magnified view of the (015) peaks for Bi_2Te_3 (at 27.7°) and Bi_2Se_3 (at 29.3°).

well-defined hexagonal structure with an extended lateral dimension of ~300 nm.

Because BS and BT are isomorphic and have similar lattice distances, compound materials (Bi_2SexTe_{3-x}) may form at the interface between the two. XRD measurements were performed on the BS@BT nanoplates ([BS]:[BT] = 1:4) to check for the presence of the compounds. Higher reaction temperatures (180, 200 °C) were also employed to facilitate the mutual diffusion between BS and BT, whereas the same overall reaction time (24 h) was used. Figure S6 in the Supporting Information shows that the same single-crystalline BS@BT nanoplates are obtained for all reaction temperatures at or above 160 °C. In Figure 6A, the XRD diffractograms are composed of two sets of peaks characteristic of pure BS (vertical black lines) and pure BT (vertical red lines). The diffractograms do not vary with the reaction temperature, which means that the crystal structure of the nanoplates, and the BS−BT interface in particular, does not change. Figure 6B shows a magnified view of the region between 26° and 32°, where the peaks at 27.7° and 29.3° are assigned to pure BT and pure BS, respectively. Although the possibility to form $Bi_2Se_xTe_{3-x}$ solid solution at the interface cannot be excluded categorically, the XRD results together with the SAED pattern in Figure 5B suggest that mutual diffusions of Se and Te were very limited at these reaction temperatures. These results are consistent with our previous report that mixed BS and BT nanoflakes retain their pure crystalline structure even after spark plasma sintering at 250 °C.[37]

Bi_2Se_3@Bi_2Te_3@Bi_2Se_3 Double-Shell Nanoplates. The as-synthesized BS@BT core/shell nanoplates ([BS]:[BT] = 1:4)

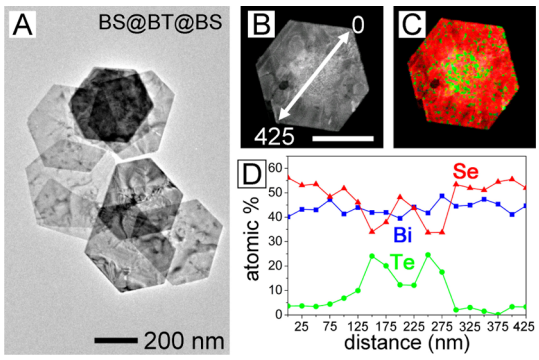

Figure 7. (A) Bright-field transmission electron micrograph, (B) high-angle annular dark field scanning transmission electron micrograph, and (C) the corresponding energy dispersive X-ray spectroscopy (EDS) map of Bi_2Se_3@Bi_2Te_3@Bi_2Se_3 ([BS]:[BT]:[BS] = 1:4:32) double-shell nanoplates. (D) Elemental profiles obtained by EDS along the arrow shown in panel (B). The scale bar in panel (B) represents 200 nm.

were used as seeds for the synthesis of BS@BT@BS double-shell nanoplates. The solution of as-synthesized BS@BT nanoplates was used without any precipitation. The precursors, acetic acid, PVP, and hydroxylamine were dissolved at room temperature in the solution, which was then kept at 160 °C for 24 h. The effect of two different molar ratios, [BS]:[BT]:[BS] = 1:4:16 and 1:4:32, were compared on the dimensions of the resulting BS layer. Figure 7 presents the characteristics of the nanoplates obtained with the 1:4:32 molar ratio. The nanoplates have a well-defined hexagonal structure (Figure 7A), 400 ± 35 nm wide and 14 ± 6 nm thick (Supporting Information, Figure S7A,B), with a proportionally greater variability in thickness than in width. The elemental distributions in these nanoplates are shown in Figure 7B−D. Whereas Te is only detected in their central parts, Se and Bi are present both at very center and the peripheral region. EDS map image clearly shows the alternate color change from red, green to red, along the lateral direction of the nanoplate, confirming that nanoplate comprises BS core (red), BT primary shell (green), and BS double shell (red) (Figure 7C). The formation of double-shell nanoplates is further examined by elemental profile (Figure 7D), showing two highest intensity peaks (~25%) of elemental Te in the middle region along with ~30% of Se. The amount of Se in this area is due to the overgrowth of Se onto basal planes of BS@BT nanoplates during the growth for BS@BT@BS nanoplates. These distributions are characteristic of the formation of BS@BT@BS double-shell nanoplates. The thickness of the nanoplates (Supporting Information, Figure S7) and the elemental maps suggest that an average of 6 quintuple BS layers is coated on the BT surface of the BS@BT nanoplates. The double-shell nanoplates produced with the 1:4:16 molar ratio also have a well-defined crystalline structure (Supporting Information, Figure S8), but they are not as wide (340 ± 25 nm) as those obtained with the 1:4:32 molar ratio. Their thickness, 9 ± 3 nm

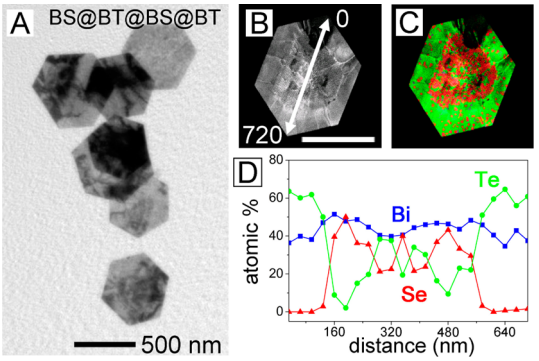

Figure 8. (A) Transmission electron micrograph, (B) high-angle annular dark field scanning transmission electron micrograph, and (C) the corresponding energy dispersive X-ray spectroscopy (EDS) map of Bi_2Se_3@Bi_2Te_3@Bi_2Se_3@Bi_2Te_3 ([BS]:[BT]:[BS]:[BT] = 1:4:32:48) multishell nanoplates. (D) Elemental profiles obtained by EDS along the arrow shown in panel (B). The scale bar in panel (B) represents 500 nm.

(Supporting Information, Figure S7C) indicates that one to three BS layers are coated on the top and bottom faces of the BS@BT nanoplates.

Bi_2Se_3@Bi_2Te_3@Bi_2Se_3@Bi_2Te_3 Multishell Nanoplates. The as-synthesized BS@BT@BS nanoplates were then used as seed crystals for the growth of multishell nanoplates. Figure 8A shows typical TEM images of the structures synthesized at a molar ratio of [BS]:[BT]:[BS]:[BT] = 1:4:32:48. The nanoplates are now 620 ± 54 nm wide and 20 ± 7 nm thick (Supporting Information, Figure S9), indicating that around four QLs of BT are coated on the double-shell nanoplates. Note that the variation in thickness arises during the synthesis of double-shell nanoplates. The elemental analysis in Figure 8B–D shows that the peripheral regions consist of pure BT. Alternating Se and Te peaks are observed in the line profiles of Figure 8D, arranged Se → Te → Se → Te from the center outward. In Figure 9A furthermore, the electron diffraction pattern obtained from a single nanoplate shows two 6-fold symmetric sets of spots with the same orientation, which are indexed to the (11$\bar{2}$0) lattice planes of pure BS (the outer set) and pure BT (the inner set). The small lattice mismatch of 4.5% for the lateral planes (11$\bar{2}$0) between BS and BT allows epitaxial growth. Moiré pattern was observed in the area where the outer BT shell and the inner BS shell are superimposed (Figure 9B). The length (L) of the Moiré pattern depends on the orientation and lattice mismatch between BS and BT layers. Assuming that the angle is 0°, then the interval length of the Moiré pattern is defined as $L = P_{BT}P_{BS}/(P_{BT} - P_{BS})$, where P_{BT} and P_{BS} are the lattice constants of the (11$\bar{2}$0) planes for BT and BS, respectively.[49] The interval of the Moiré pattern from the equation was calculated to be 4.62 nm based on the values (P_{BT} = 0.22 nm, P_{BS} = 0.21 nm). The observed length (L) of 4.9 ± 0.2 nm in Figure 9B was in a good agreement with the calculated value, which supports the occurrence of epitaxial growth of the (11$\bar{2}$0) planes between BS and BT. The pattern in the

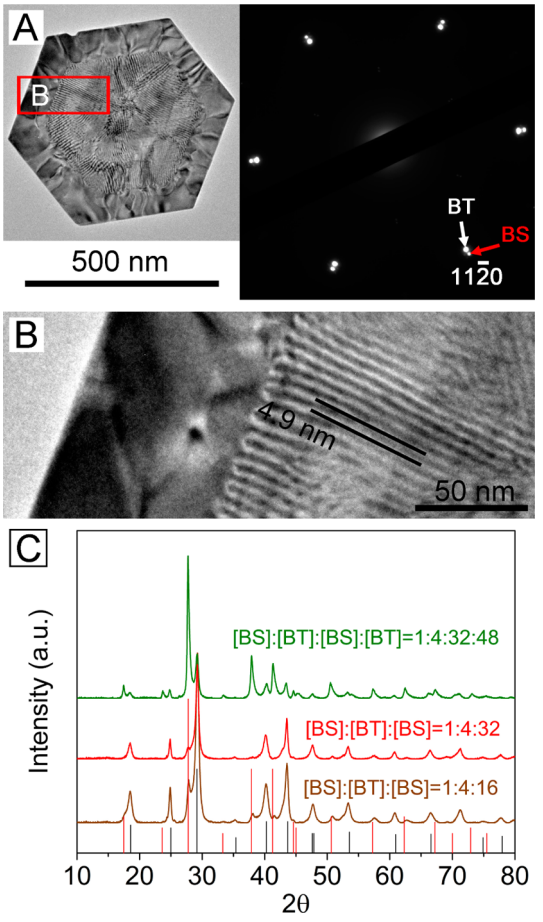

Figure 9. (A) Typical transmission electron micrograph (TEM) of a single Bi_2Se_3@Bi_2Te_3@Bi_2Se_3@Bi_2Te_3 multishell nanoplate ([BS]:[BT]:[BS]:[BT] = 1:4:32:48) and the corresponding electron diffraction pattern along the [0001] zone axis. (B) Magnified TEM image of the solid red rectangle in panel A, showing a Moiré patterns between BS and BT lattices. (C) X-ray diffractograms obtained from double-shell and multishell nanoplates with vertical lines showing JCPDS peaks positions for rhombohedral Bi_2Se_3 (33-0214, black) and Bi_2Te_3 (15-0863, red).

corresponding XRD diffractogram (Figure 9C) can be decomposed into peaks characteristic of pure rhombohedral BS and pure BT. The fact that the strongest peak for the double-shell nanoplates is assigned to BS and that for the multishell nanoplates is assigned to BT further confirms the successful assembly of multishell nanoplates without any compound formation at the interfaces.

Thermoelectric Properties of Bulk Pellets Made of Bi_2Se_3 and Bi_2Se_3@Bi_2Te_3 Nanoplates. The surfactant PVP attached on the as-synthesized nanoplates was removed by following the previous method reported by Wu's group.[50] Experimental details are found in the Experimental Section. The BS and BS@BT powders were sintered by spark plasma sintering (SPS) under 30 MPa at 250 °C for 2 min. Xiong and co-workers revealed that 250 °C SPS temperature was most effective for their $Bi_2Te_{3-x}Se_x$ nanoplatelet composites.[39] They observed significant grain growth and interface rearrangement at higher temperatures (*e.g.*, 280 and 350 °C), which caused

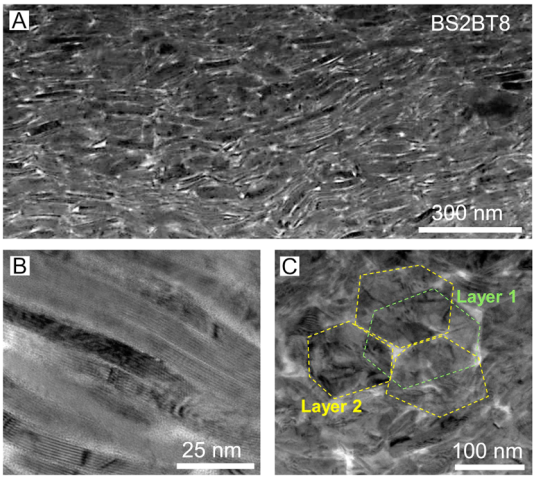

Figure 10. TEM images of the sintered pellet made of the BS2BT8 nanoplates. The TEM samples were obtained by focused ion-beam. (A) A large area cross-section image and (B) a magnified cross-section image. The magnified image shows the layer-by-layer stacking of the nanoplates in the perpendicular direction to the pressure applied during the sintering. (C) In-plain TEM image of the same sintered pellet, showing overlay of the nanoplates.

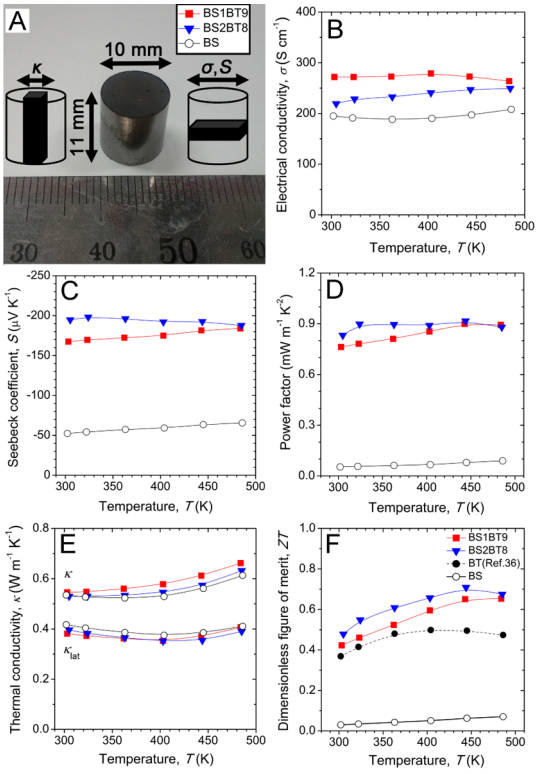

Figure 11. (A) A photograph of the sintered cylinder-shaped pellet sample prepared by spark plasma sintering. The dimensions are denoted (10 mm in diameter and 11 mm in height). The cylinder pellet was cut off into rectangular parallelepiped. The thermoelectric properties were measured in the perpendicular direction to the pressure applied to the pellet. Temperature dependence of (B) electrical conductivities, (C) Seebeck coefficients, (D) power factor, (E) thermal conductivities, and (F) the dimensionless thermoelectric figure of merit (ZT) of the pellets made of BS, BS2BT8, and BS1BT9. The dashed line in panel F shows the ZT values from the surfactant-free BT nanoplates reported in ref 36.

decrease in thermoelectric power. Similarly, we found that 250 °C is the most effective SPS temperature for retaining the core/shell heterostructure without phase change at the interface and for preventing grain growth during sintering. The sintered samples were denoted by BS (Bi_2Se_3), BS2BT8 (BS@BT, [BS]:[BT] = 1:4), and BS1BT9 (BS@BT, [BS]:[BT] = 1:9) according to the relative molar ratios between BS and BT. The lateral dimensions of BS were identical because the core–shell nanoplates were prepared from the same BS seeds. The phase purity and crystal structure of the sintered pellets were examined by XRD (Supporting Information, Figure S10). In the XRD diffractograms obtained from the sintered pellets, all the peaks were perfectly indexed to those of BT and BS lattices without any peak shift, which indicates that compound formation or oxidation did not take place, and if any in a very limited amount, during the SPS process. This result was further confirmed from the microstructure of the SPS pellets. The cross-sectional TEM image of the sintered BS2BT8 sample is shown in Figure 10A. Figure 10B is a cross-section image and Figure 10C is an in-plane image of the pellet. The nanoplates were stacked along the $(11\bar{2}0)$ plane. They were aligned in the perpendicular direction to the pressure applied during the SPS, forming a layer-by-layer structure. Grain growth of nanoplates was not observed due to the low sintering temperature (250 °C) during relatively short time (2 min). Very similar stacking of nanoplates and alignment was observed in the sintered BS1BT9 pellet without any grain growth (Supporting Information, Figure S10).

Since the specific alignment of the nanoplates can affect the thermoelectric properties depending on the measurement direction, degree of orientation in all pellets was quantitatively calculated. The texture fraction of the $\{00l\}$ planes was evaluated using Lotgering factor (f) calculated from the X-ray diffractograms[51] (Supporting Information Figure S10) obtained by irradiating X-ray in the perpendicular direction to the SPS pressure. The f for $\{00l\}$ planes is defined as $f_{00l} = (p_{00l} - p_0)/(1 - p_0)$, where $p_{00l} = \Sigma I_{00l}/\Sigma I_{hkl}$ and $p_0 = \Sigma I^0_{00l}/\Sigma I^0_{hkl}$ with I_{hkl} and I^0_{hkl}. I_{hkl} and I^0_{hkl} are the intensities of (h k l) peaks for the textured and randomly oriented samples, respectively. The f_{00l} values for BS, BS2BT8, and BS1BT9 samples were 0.36, 0.27, and 0.30. The orientation of nanoplates in the pellets affects the physical properties along the directions. To provide practical thermoelectric characteristics of the pellets, the measurements for thermal conductivity (κ), electrical conductivity (σ), and Seebeck coefficient (S) were carried out in perpendicular to the SPS press direction to acquire the accurate thermoelectric properties (Figure 11A). The Figure 11B shows the electric conductivity (σ) for the bulks of BS@BT core–shell nanoplates, revealing the monotonic decrease with the increase of BS composition in the whole the

temperature. The σ values of the samples were in the range of 220−270 S/cm, which values were relatively low due to the electron carrier scattering at the interfaces. The negative values of the Seebeck coefficient (S) indicate that the major charge carriers are electrons (Figure 11C). The absolute value of S of the BS2BT8 nanoplates was larger than that of BS1BT9 due to its lower σ. It should be noted that increase of Seebeck coefficient in BS2BT8 was large considering the level of the decrease in σ, indicating that potential barrier scattering at high density of BS−BT interfaces enhanced the Seebeck coefficient. This is clearly seen in the plot of power factor (σS^2) as shown in Figure 11D. The maximum power factor (0.9 mW/m·K^2 at 450 K) in this study was obtained in the BS2BT8 core−shell nanoplates. To clarify the mechanism, we calculated carrier concentration (n_c) and mobility (μ) at 300 K. The n_c and μ values were 1.61 × 10^{19} cm^{-3} and 85 cm^2/V·s for BS2BT8 and 1.73 × 10^{19} cm^{-3} and 98 cm^2/V·s for BS1BT9, respectively. The order of 10^{19} cm^{-3} carrier density is similar to the values reported for high performance thermoelectric materials.[38] Considering the smaller size of BS2BT8 than BS1BT9 with the same size of the core BS, the larger volume fraction of BS in the BS2BT8 results in a smaller electron mobility. Another possibility is scattering of low-energy electrons passing through the densely distributed interfaces (BT−BT and BS−BT), which may further improve σS^2 by increasing the density of BS−BT interface. This trend of the σ and S has coincidence with our previous work in which pure BS nanoplates and pure BT nanoplates were mixed homogeneously.[37]

Figure 11E shows the thermal conductivity (κ). Compared to κ of Bi_2Te_3 bulk with microsized grains (~1.5 W/m·K at 300 K), κ values of the core−shell nanoplates were significantly lower (0.53−0.55 W/m·K at 300 K). Because κ contains electronic contribution ($\kappa_{ele} = \kappa - \kappa_{lat}$, where κ_{lat} is the lattice thermal conductivity) which is determined by the Wiedemann−Franz law ($\kappa_{ele} = LT\sigma$, where L is the Lorenz number), we calculated κ_{lat} with L = 2.0 × 10^{-8} V^2/K^2 to clarify the thermal transport behavior. The BS2BT8 pellets have a larger number density of interfaces (BS−BT interface and BT−BT grain boundary) than BS1BT9 pellet, so a lower lattice thermal conductivity (κ_{lat}) is expected in the BS2BT8 pellets. But significantly low values of lattice thermal conductivity (0.38−0.40 W/m·K at 300 K) were obtained in both pellets, which indicates that the number of interfaces and grain boundaries for phonon scattering are saturated in the BS1BT9 pellet. Such low κ_{lat} values are attributed to the intensified phonon scattering at the interfaces (BT−BT grain boundary and BS−BT phase boundary). And also, low-energy electrons would be scattered more at the BS−BT interface, leading to improvement of power factor in BS2BT8. We believe that power factor might be further raised by optimizing the ratio of number densities of BS−BT interface and BT−BT boundary. Characterization of the interfaces and the optimization are to be studied in the future. This simultaneous improvement in electronic and thermal transport properties resulted in high figure of merit (ZT) of BS2BT8 (~0.71 at 450 K) (Figure 11F). Note that the ZT of BT samples in Figure 11F (black dashed line) was denoted from our pervious result in which a pellet of surfactant-free BT nanoflakes prepared with the same process condition was used. It is notable that the orientations of the BT nanoflakes were very similar to those in this study.[37]

CONCLUSION

Heterostructured 2D chalcogenides have been produced using consecutive epitaxial growth of Bi_2Te_3 (BT) and Bi_2Se_3 (BS), starting from BS nanoplates and grown up to multishell BS@BT@BS@BT nanoplates. The BT nanoparticles generated rapidly in the reaction solution attach preferentially on the sides of the seed BS nanoplates rather than on their basal planes. The nanoparticles near the edges of the nanoplates reorganize, allowing epitaxial growth and creating well-defined single-crystalline hexagonal structures. The migration of the nanoparticles deposited on the basal planes to the edges of the nanoplates contributes to lateral growth and leads to a uniform coat on the BS surface. The mechanism through which BS is coated on the BT layer is identical. The lateral dimensions and the relative core and shell widths of the heterostructure can be controlled by adjusting the molar ratios of the precursors added to the seed nanoplate solution. The BS@BT core−shell nanoplates allowed homogeneous distribution of BS nanoplates in a BT matrix. The maximum ZT was found to be ~0.71 at 450 K for the bulk of BS@BT core−shell nanoplates with an atomic ratio of ([BS]:[BT] = 1:4). The improved ZT compared from that of the bulk of pure BT nanoplates is due to a simultaneous improvement in electronic and thermal transport properties.

EXPERIMENTAL SECTION

Materials. The chemicals used in this study were sodium selenite (Na_2SeO_3, 99%, Aldrich), sodium tellurite (Na_2TeO_3, 99%, Aldrich), bismuth nitrate pentahydrate ($Bi(NO_3)_3 \cdot 5H_2O$, 99.99+ %, Aldrich), hydroxylamine (NH_2OH, 50 wt % in H_2O, Aldrich), poly(vinylpyrrolidone) (PVP, M_w = 55 000 g/mol Da, Sigma-Aldrich), acetic acid glacial (CH_3COOH ≥99%, Duksan, Korea), acetone (C_3H_6O ≥ 99.8%, Sigma-Aldrich), and ethylene glycol (EG ≥99%, J. T. Baker). DI water was obtained using an 18-MΩ (SHRO-plus DI) system.

Synthesis of the Bi_2Se_3 Seed Nanoplates. A solution of PVP (0.4 g in 20 mL of EG) was poured into a 250 mL round-bottom flask, followed by solutions of sodium selenite (0.121 g in 20 mL of EG), bismuth nitrate pentahydrate (0.226 g in 10 mL of EG), and

acetic acid (12 mL), all added under magnetic stirring at room temperature. The flask was sealed using a septum and heated to 165 °C under nitrogen atmosphere. As the reaction temperature was increased, the transparent solution became light yellow. Upon rapid injection of hydroxylamine solution (1.2 mL in 10 mL of EG) into the mixture at 165 °C, the solution immediately turned dark purple, indicating the formation of Bi_2Se_3 nanoplates. The reaction completed within 5 min, but was allowed to proceed for 10 further minutes before being cooled down to room temperature.

Synthesis of the Bi_2Se_3@Bi_2Te_3 Core–Shell Nanoplates. The molar ratio ([BS]:[BT]) was adjusted according to the desired lateral size of the core/shell nanoplates. With a 1:4 molar ratio for example, stoichiometric amounts of sodium tellurite (0.62 g in 70 mL of EG) and bismuth nitrate pentahydrate (0.91 g in 30 mL of EG) were added to the as-synthesized BS-seed suspension at room temperature. Note that the BS-seed suspension was used directly after cooling without any precipitation. PVP (0.8 g in 40 mL of EG) and hydroxylamine (2.4 mL in 10 mL of EG) solutions were further added to the mixture under magnetic stirring at room temperature. The reaction chamber was sealed and heated to 160 °C under nitrogen atmosphere. The reaction took 24 h to complete. The suspension was then cooled down to room temperature and used for the synthesis of double-shell nanoplates without any further purification steps.

Synthesis of the Bi_2Se_3@Bi_2Te_3@Bi_2Se_3 Double-Shell Nanoplates. In this study, two molar ratios were used, [BS]:[BT]:[BS] = 1:4:16 and 1:4:32, to prepare nanoplates with different dimensions. Sodium selenite (0.242 g in 40 mL of EG), bismuth nitrate pentahydrate (0.452 g in 15 mL of EG), PVP (0.4 g in 20 mL of EG), hydroxylamine (0.8 mL in 10 mL of EG), and acetic acid (14 mL) solutions were poured into a 250 mL round-bottom flask under magnetic stirring. An identical mixture was prepared in another flask. One-eighth of the as-prepared Bi_2Se_3@Bi_2Te_3 core/shell suspension was added to one of the flasks and 1/16 to the other for the 1:4:16 and 1:4:32 molar ratios, respectively. The flasks were then sealed and kept at 160 °C for 24 h for the reaction to proceed. The solutions were then cooled to room temperature and kept in the flasks for the synthesis of multishell nanoplates without any precipitation steps.

Synthesis of the Bi_2Se_3@Bi_2Te_3@Bi_2Se_3@Bi_2Te_3 Multishell Nanoplates. A molar ratio [BS]:[BT]:[BS]:[BT] = 1:4:32:48 was used. A solution of sodium tellurite (0.152 g in 20 mL of EG), bismuth nitrate pentahydrate (0.226 g in 10 mL of EG), PVP (0.2 g in 10 mL of EG), hydroxylamine (1.2 mL in 10 mL of EG), and acetic acid (1 mL) was prepared in a 250 mL round-bottom flask. One-third of the as-synthesized BS@BT@BS nanoplate suspension ([BS]:[BT]:[BS] = 1:4:32) was then added to the mixture at room temperature. The resulting solution was heated to 160 °C and kept for 24 h under nitrogen atmosphere. The final product was collected by centrifugation (~11 000 rpm, 10 min) and washed three times with DI water and ethanol.

Fabrication of Pelletized Bulk Samples by Spark Plasma Sintering (SPS). Spark plasma sintering (SPS) was employed to prevent the grain growth of atomic diffusion between the interfaces of the nanoplates. Prior to the SPS process, the surfactant PVP used to stabilize the nanoplates was removed with a diluted hydrazine solution.[50] The as-synthesized nanoplates were redispersed in ethanol. Hydrazine hydrate was added to the dispersion. Volume fraction of hydrazine hydrate was 15% of the total volume of the dispersion solution. The mixture solution was stirred vigorously until all the nanoplates were precipitated. The precipitates were collected and washed by centrifugation (15 000 rpm, 10 min) three times with a mixture of ethanol and acetone. It was dried at room temperature under vacuum for several hours and then stored in a glovebox to prevent oxidation of the nanoplates. The dry powders were pelletized by spark plasma sintering (SPS) under 30 MPa at 250 °C for 2 min under a vacuum. The pellets were cylinders with 10 mm in diameter and 11 mm in height.

Measurements of Thermoelectric Properties. The electrical conductivities and Seebeck coefficients were measured from 300 to 480 K with a thermoelectric measurement system (ZEM-3, ULVAC, Japan) in He atmosphere. The thermal conductivities ($\kappa = \rho_s \cdot C_p \cdot \lambda$) were calculated from measurements taken separately. Sample density (ρ_s) was measured by Archimedes method. The heat capacity (C_p) and thermal diffusivity (λ) values were measured under vacuum by laser-flash method (TC-9000, ULVAC, Japan). The carrier concentration (n_c) and mobility (μ) were estimated from the Hall resistivity, which was measured in the van der Pauw configuration.

Characterization. Samples were analyzed by transmission electron microscopy (TEM, JEM-2100F and JEM-2011HC, JEOL) at an accelerating voltage of 200 kV, energy dispersive X-ray spectrometry (EDS, INCA X-sight 7421, Oxford Instruments), and by X-ray diffraction (XRD, D/MAX II, Rigaku) with Cu Kα radiation (λ = 0.1542 nm). The topologies of the nanoplates were examined by atomic force microscopy (AFM, Dimension 3100, Digital Instruments Co.). The bismuth, tellurium, and selenium contents were measured by inductively coupled plasma optical emission spectrometry (ICP-OES, Optima 8300, PerkinElmer) using three ICP standards (0.0, 2.0, and 20.0 ppm of Bi and Te; 0.0, 1.0, and 10.0 ppm of Se prepared in 5 wt % HNO_3 background solutions.

Conflict of Interest: The authors declare no competing financial interest.

Supporting Information Available: Analytical data (TEM, AFM, XRD, and compositional analysis) are included. The Supporting Information is available free of charge on the ACS Publications website at DOI: 10.1021/nn507250r.

Acknowledgment. This research was supported partly by Samsung Research Funding Center of Samsung Electronics under Project Number SRFC-MA1301-07.

REFERENCES AND NOTES

1. Carbone, L.; Cozzoli, P. D. Colloidal Heterostructured Nanocrystals: Synthesis and Growth Mechanisms. *Nano Today* **2010**, *5*, 449–493.
2. Donegá, C. d. M. Synthesis and Properties of Colloidal Heteronanocrystals. *Chem. Soc. Rev.* **2011**, *40*, 1512–1546.
3. Min, Y.; Moon, G. D.; Kim, C.-E.; Lee, J.-H.; Yang, H.; Soon, A.; Jeong, U. Solution-based Synthesis of Anisotropic Metal Chalcogenide Nanocrystals and their Applications. *J. Mater. Chem. C* **2014**, *2*, 6222–6248.
4. Fan, Z.; Huang, X.; Tan, C.; Zhang, H. Thin Metal Nanostructures: Synthesis, Properties and Applications. *Chem. Sci.* **2015**, *6*, 95–111.
5. Zhang, X.; Xie, Y. Recent Advances in Free-standing Two-dimensional Crystals with Atomic Thickness: Design, Assembly and Transfer Strategies. *Chem. Soc. Rev.* **2013**, *42*, 8187–8199.
6. Chhowalla, M.; Shin, H. S.; Eda, G.; Li, L. J.; Loh, K. P.; Zhang, H. The Chemistry of Two-dimensional Layered Transition Metal Dichalcogenide Nanosheets. *Nat. Chem.* **2013**, *5*, 263–275.
7. Butler, S. Z.; Hollen, S. M.; Cao, L.; Cui, Y.; Gupta, J. A.; Gutiérrez, H. R.; Heinz, T. F.; Hong, S. S.; Huang, J.; Ismach, A. F.; et al. Progress, Challenges, and Opportunities in Two-dimensional Materials Beyond Graphene. *ACS Nano* **2013**, *7*, 2898–2926.
8. Rao, C. N. R.; Ramakrishna Matte, H. S. S.; Maitra, U. Graphene Analogues of Inorganic Layered Materials. *Angew. Chem., Int. Ed.* **2013**, *52*, 13162–13185.
9. Lin, Z.; Chen, Y.; Yin, A.; He, Q.; Huang, X.; Xu, Y.; Liu, Y.; Zhong, X.; Huang, Y.; Duan, X. 1.Solution Processable Colloidal Nanoplates as Building Blocks for High-Performance Electronic Thin Films on Flexible Substrates. *Nano Lett.* **2014**, *14*, 6547–6553.
10. Koski, K. J.; Cui, Y. The New Skinny in Two-Dimensional Nanomaterials. *ACS Nano* **2013**, *7*, 3739–3743.
11. Li, H.; Wu, J.; Yin, Z.; Zhang, H. Prepartion and Applications of Mechanically Exfoliated Single-Layer and Multilayer MoS_2 and WSe_2 Nanosheets. *Acc. Chem. Res.* **2014**, *47*, 1067–1075.

12. Huang, X.; Tan, C.; Yin, Z.; Zhang, H. 25th Anniversary Article: Hybrid Nanostructures Based on Two-Dimensional Nanomaterials. *Adv. Mater.* **2014**, *26*, 2185–2204.
13. Huang, X.; Zeng, Z.; Zhang, H. Metal Dichalcogenide Nanosheets: Preperation, Properties and Applications. *Chem. Soc. Rev.* **2013**, *42*, 1934–1946.
14. Yu, T.; Lim, B.; Xia, Y. Aqueous-phase Synthesis of Single-crystal Ceria Nanosheets. *Angew. Chem., Int. Ed.* **2010**, *49*, 4484–4487.
15. Zhang, X.; Zhang, J.; Zhao, J.; Pan, B.; Kong, M.; Chen, J.; Xie, Y. Half-metallic Ferromagnetism in Synthetic Co_9Se_8 Nanosheets with Atomic Thickness. *J. Am. Chem. Soc.* **2012**, *134*, 11908–11911.
16. Jeong, S.; Yoo, D.; Jang, J.-t.; Kim, M.; Cheon, J. Well-defined Colloidal 2-D Layered Transition-metal Chalcogenide Nanocrystals *via* Generalized Synthetic Protocols. *J. Am. Chem. Soc.* **2012**, *134*, 18233–18236.
17. Li, L.; Chen, Z.; Hu, Y.; Wang, X.; Zhang, T.; Chen, W.; Wang, Q. Single-layer Single-crystalline SnSe Nanosheets. *J. Am. Chem. Soc.* **2013**, *135*, 1213–1216.
18. Coleman, J. N.; Lotya, M.; O'Neill, A.; Bergin, S. D.; King, P. J.; Khan, U.; Young, K.; Gaucher, A.; De, S.; Smith, R. J.; et al. Two-dimensional Nanosheets Produced by Liquid Exfoliation of Layered Materials. *Science* **2011**, *331*, 568–571.
19. Yang, J.; Son, J. S.; Yu, J. H.; Joo, J.; Hyeon, T. Advance in the Colloidal Synthesis of Two-dimensional Semiconductor Nanoribbons. *Chem. Mater.* **2013**, *25*, 1190–1198.
20. Yang, D.; Lu, Z.; Rui, X.; Huang, X.; Li, H.; Zhu, J.; Zhang, W.; Lam, Y. M.; Hng, H. H.; Zhang, H.; Yan, Q. Synthesis of Two-Dimensional Transition-Metal Phosphastes with Highly Ordered Mesoporous Structures for Lithium-Ion Battery Applications. *Angew. Chem., Int. Ed.* **2014**, *53*, 9352–9355.
21. Wu, X.-J.; Huang, X.; Qi, X.; Li, H.; Li, B.; Zhang, H. Copper-Based Ternary and Quaternary Semiconductor Nanoplates: Templated Synthesis, Characterization, and Photoelectrochemical Properties. *Angew. Chem., Int. Ed.* **2014**, *53*, 8929–8933.
22. Wu, X.-J.; Huang, X.; Liu, J.; Li, H.; Yang, J.; Li, B.; Huang, W.; Zhang, H. Two-Dimensional CuSe Nanosheets with Micro-scale Lateral Size: Synthesis and Template-Assisted Phase Transformation. *Angew. Chem., Int. Ed.* **2014**, *53*, 5083–5087.
23. Zhang, J.; Peng, Z.; Soni, A.; Zhao, Y.; Xiong, Y.; Peng, B.; Wang, J.; Dresselhaus, M. S.; Xiong, Q. Raman Spectroscpy of Few-Quintuple Layer Topological Insulator Bi_2Se_3 Nanoplatelets. *Nano Lett.* **2011**, *11*, 2407–2414.
24. Tessier, M. D.; Spinicelli, P.; Dupont, D.; Patriarche, G.; Ithurria, S.; Dubertret, B. Efficient Exciton Concentrators Built from Colloidal Core/Crown CdSe/CdS Semiconductor Nanoplatelets. *Nano Lett.* **2014**, *14*, 207–213.
25. Mahler, B.; Nadal, B.; Bouet, C.; Patriarche, G.; Dubertret, B. Core/Shell Colloidal Semiconductor Nanoplatelets. *J. Am. Chem. Soc.* **2012**, *134*, 18591–18598.
26. Prudnikau, A.; Chuvilin, A.; Artemyev, M. CdSe-CdS Nanoheteroplatelets with Efficient Photoexcitation of Central CdSe Region through Epitaxially Grown CdS Wings. *J. Am. Chem. Soc.* **2013**, *135*, 14476–14479.
27. Lauhon, L. J.; Gudiksen, M. S.; Wang, D.; Lieber, C. M. Epitaxial Core-Shell and Core-Multishell Nanowire Heterostructures. *Nature* **2002**, *420*, 57–61.
28. Asikainen, T.; Ritala, M.; Leskelä, M. Growth of In_2S_3 Thin Films by Atomic Layer Epitaxy. *Appl. Surf. Sci.* **1994**, *82*−*83*, 122–125.
29. Miikkulainen, V.; Leskelä, M.; Ritala, M.; Puurunen, R. L. Crystallinity of Inorganic Films Grown by Atomic Layer Deposition: Overview and General Trends. *J. Appl. Phys.* **2013**, *113*, 021301.
30. Bouet, C.; Tessier, M. D.; Ithurria, S.; Mahler, B.; Nadal, B.; Dubertret, B. Flat Colloidal Semiconductor Nanoplatelets. *Chem. Mater.* **2013**, *25*, 1262–1271.
31. Min, Y.; Kwak, J.; Soon, A.; Jeong, U. Nonstoichiometric Nucleation and Growth of Multicomponent Nanocrystals in Solution. *Acc. Chem. Res.* **2014**, *47*, 2887–2893.
32. Wang, L.; Yamauchi, Y. Autoprogrammed Synthesis of Triple-layered Au@Pd@Pt Core-Shell Nanoparticles Consisting of a Au@Pd Bimetallic Core and Nanoporous Pt Shell. *J. Am. Chem. Soc.* **2010**, *132*, 13636–13638.
33. Qiu, F.; Liu, G.; Li, L.; Wang, Y.; Xu, C.; An, C.; Chen, C.; Xu, Y.; Huang, Y.; Wang, Y.; et al. Synthesis of Triple-Layered Ag@Co@Ni Core-Shell Nanoparticles for the Catalytic Dehydrogenation of Ammonia Borane. *Chem. - Eur. J.* **2014**, *20*, 505–509.
34. Johnson, N. J. J.; van Veggel, F. C. J. M. Lanthanide-Based Heteroepitaxial Core−Shell Nanostructures: Compressive *versus* Tensile Strain Asymmetry. *ACS Nano* **2014**, *8*, 10517–10527.
35. Koo, B.; Korgel, B. A. Coalescence and Interface Diffusion in Linear CdTe/CdSe/CdTe Heterojunction Nanorods. *Nano Lett.* **2008**, *8*, 2490–2496.
36. Min, Y.; Moon, G. D.; Kim, B. S.; Lim, B.; Kim, J.-S.; Kang, C. Y.; Jeong, U. Quick, Controlled Synthesis of Ultrathin Bi_2Se_3 Nanodiscs and Nanosheets. *J. Am. Chem. Soc.* **2012**, *134*, 2872–2875.
37. Min, Y.; Roh, J. W.; Yang, H.; Park, M.; Kim, S. I.; Hwang, S.; Lee, S. M.; Lee, K. H.; Jeong, U. Surfactant-free Scalable Synthesis of Bi_2Te_3 and Bi_2Se_3 Nanoflakes and Enhanced Thermoelectric Properties of their Nanocomposites. *Adv. Mater.* **2013**, *25*, 1425–1429.
38. Soni, A.; Yanyuan, Z.; Ligen, Y.; Aik, M. K.; Dresselhaus, M. S.; Xiong, Q. Enhanced thermoelectric properties of solution grown $Bi_2Te_{(3-x)}Se_{(x)}$ nanoplatelet composites. *Nano Lett.* **2012**, *12*, 1203–1209.
39. Soni, A.; Shen, Y.; Yin, M.; Zhao, Y.; Yu, L.; Hu, X.; Dong, Z.; Khor, K. A.; Dresselhaus, M. S.; Xiong, Q. Interface driven energy filtering of thermoelectric power in spark plasma sintered $Bi_2Te_{2.7}Se_{0.3}$ nanoplatelet composites. *Nano Lett.* **2012**, *12*, 4305–4310.
40. Sun, Y.; Cheng, H.; Gao, S.; Liu, Q.; Sun, Z.; Xiao, C.; Wu, C.; Wei, S.; Xie, Y. Atomically Thick Bismuth Selenide Freestanding Single Layers Achieving Enhanced Thermoelectric Energy Harvesting. *J. Am. Chem. Soc.* **2012**, *134*, 20294–20297.
41. Mehta, R. J.; Zhang, Y.; Karthik, C.; Singh, B.; Siegel, R. W.; Borca-Tasciuc, T.; Ramanath, G. A new class of doped nanobulk high-figure-of-merit thermoelectrics by scalable bottom-up assembly. *Nat. Mater.* **2012**, *11*, 233–240.
42. Son, J. S.; Choi, M. K.; Han, M. K.; Park, K.; Kim, J. Y.; Lim, S. J.; Oh, M.; Kuk, Y.; Park, C.; Kim, S. J.; Hyeon, T. n-Type nanostructured thermoelectric materials prepared from chemically synthesized ultrathin Bi_2Te_3 nanoplates. *Nano Lett.* **2012**, *12*, 640–647.
43. Kong, D.; Dang, W.; Cha, J. J.; Li, H.; Meister, S.; Peng, H.; Liu, Z.; Cui, Y. Few-layer Nanoplates of Bi_2Se_3 and Bi_2Te_3 with Highly Tunable Chemical Potential. *Nano Lett.* **2010**, *10*, 2245–2250.
44. Kong, D.; Koski, K. J.; Cha, J. J.; Hong, S. S.; Cui, Y. Ambipolar Field Effect in Sb-Doped Bi_2Se_3 Nanoplates by Solvothermal Synthesis. *Nano Lett.* **2013**, *13*, 632–636.
45. Coelho, P. M.; Ribeiro, G. A. S.; Malachias, A.; Pimentel, V. L.; Silva, W. S.; Reis, D. D.; Mazzoni, M. S. C.; Magalhães-Paniago, R. Temperature-Induced Coexistence of a Conducting Bilayer and the Bulk-Terminated Surface of the Topological Insulator Bi_2Te_3. *Nano Lett.* **2013**, *13*, 4517–4521.
46. Snyder, G. J.; Toberer, E. S. Complex Thermoelectric Materials. *Nat. Mater.* **2008**, *7*, 105–114.
47. Ko, D.-K.; Kang, Y.; Murray, C. B. Enhanced Thermopower *via* Carrier Energy Filtering in Solution-Processable Pt-Sb_2Te_3 Nanocomposites. *Nano Lett.* **2011**, *11*, 2841–2844.
48. Hirsch, P. B.; Howie, A.; Nicholson, R. B.; Pashley, D. W.; Whelan, M. J. *Electron Microscopy of Thin Crystals*; Plenum Press: New York, 1965; pp 169−170.
49. Hermann, K. Periodic overlayers and moire Patterns: theoretical studies of geometric properties. *J. Phys.: Condens. Matter* **2012**, *24*, 314210.
50. Zhang, G.; Kirk, B.; Jauregui, L. A.; Yang, H.; Xu, X.; Chen, Y. P.; Wu, Y. Rational Synthesis of Ultrathin n-Type Bi_2Te_3 Nanowires with Enhanced Thermoelectric Properties. *Nano Lett.* **2012**, *12*, 56–60.
51. Lotgering, F. K. *J. Inorg. Nucl. Chem.* **1959**, *9*, 113–123.